Published in final edited form as:
Nat Med. 2017 July ; 23(7): 869–877. doi:10.1038/nm.4343.

Combined *Vhl*, *Trp53* and *Rb1* mutation causes clear cell renal cell carcinoma in mice

Sabine Harlander[1,2], **Désirée Schönenberger**[1], **Nora C. Toussaint**[3,4], **Michael Prummer**[3,4], **Antonella Catalano**[1,6,7], **Laura Brandt**[1], **Holger Moch**[5], **Peter J. Wild**[5], and **Ian J. Frew**[1,2,6,7]

[1]Institute of Physiology, University of Zurich, Zurich, Switzerland [2]Zurich Center for Integrative Human Physiology, University of Zurich, Zurich, Switzerland [3]NEXUS Personalized Health Technologies, ETH Zurich, Zurich, Switzerland [4]SIB Swiss Institute of Bioinformatics, Zurich, Swizerland [5]Department of Pathology and Molecular Pathology, University Hospital Zurich, Zurich, Switzerland [6]BIOSS Centre for Biological Signalling Studies, University of Freiburg, Freiburg, Germany [7]Center for Translational Cell Research, Faculty of Medicine, University of Freiburg, Freiburg, Germany

Abstract

Clear cell renal cell carcinomas (ccRCC) frequently exhibit inactivation of the *VHL* tumour suppressor gene and often harbour multiple copy number alterations in genes that regulate cell cycle progression. We show here that modelling these genetic alterations by combined renal epithelium-specific deletion of *Vhl*, *Trp53* and *Rb1* in mice caused ccRCC. These tumours arose from proximal tubule epithelial cells and shared molecular markers and mRNA expression profiles with human ccRCC. Exome sequencing revealed that mouse and human ccRCCs exhibit recurrent mutations in genes associated with the primary cilium, uncovering a mutational convergence on this organelle and implicating a subset of ccRCCs as genetic ciliopathies. Different mouse tumours responded differently to standard therapies for advanced human ccRCC, mimicking the range of clinical behaviours in the human disease. Inhibition of HIF-α transcription factors with Acriflavine as third line therapy had therapeutic effects in some tumours, providing pre-clinical evidence for further investigation of HIF-α inhibition as a ccRCC treatment. This autochthonous mouse ccRCC model represents a tool to investigate the biology of ccRCC and to identify new treatment strategies.

Corresponding Author and Address: Ian Frew, Centre for Translational Cell Research, Faculty of Medicine, University of Freiburg, Breisacherstraße 115, 79106 Freiburg, Germany, Phone: +49 761 270 71831, ian.frew@uniklinik-freiburg.de.

Author Contributions

I.J.F. and S.H. designed the study; S.H., D.S., A.C., L.B. conducted experiments; N.C.T., M.P., I.J.F., S.H. conducted bioinformatic analyses; P.J.W., H.M. conducted pathological analyses, I.J.F. wrote the manuscript with input from all authors.

Competing Financial Interests

The authors declare that there are no competing financial interests related to this publication.

Europe PMC Funders Author Manuscripts

Introduction

Kidney cancers represent approximately 2-3% of all human cancers and ccRCC accounts for roughly 70% of all renal malignancies 1. Metastatic spread of ccRCC occurs in about half of all patients and despite ongoing improvements in clinical management due to the availability of several therapeutic options in the form of targeted therapies and immune checkpoint blocking agents, 5-year survival rates for patients with metastatic disease are still only around 8-12% 2,3. 82-92% of ccRCC tumours harbour biallelic inactivation of the von Hippel-Lindau (*VHL*) tumour suppressor gene 4–6 and *VHL* mutations occur at the earliest stage of tumor formation 7. Patients with VHL disease inherit a mutant *VHL* allele and are predisposed to develop ccRCC. However, second hit *VHL* loss-of-function mutations in renal epithelial cells in VHL patients are insufficient to cause ccRCC in humans 8 and numerous renal-epithelial cell-specific *Vhl* knockout mice also failed to develop ccRCC (reviewed in 9), arguing that ccRCC formation requires mutations in addition to *VHL*. The presence of recurrent mutations in *PBRM1*, *BAP1*, *SETD2*, *KDM5C*, *PIK3CA*, *PTEN*, *MTOR* and *TP53*, as well as copy number losses of *CDKN2A* and *RB1* and gains of *MDM4* and *MYC* in human ccRCCs 6,10 argues that these genetic alterations may act cooperatively with *VHL* loss to induce ccRCC formation. Consistent with this hypothesis, kidney epithelial cell-specific co-deletion of *Vhl* with *Pten* 11, or with *Kif3a* to genetically ablate primary cilia 12, caused the formation of simple and atypical cystic lesions, mimicking the proposed precursor lesions of a subset of ccRCCs. Deletion of *Vhl* together with *Trp53* gave rise to simple and atypical cystic lesions as well as small tumours containing cells that display cytoplasmic clearing and elevated mTORC1 activity 13, recapitulating some of the cellular and molecular changes that are characteristic of human ccRCC. Similar phenotypes were observed in mice with combined *Vhl* deletion and heterozygous loss of *Bap1* 14. While these mouse models reproduce ccRCC precursor lesions and small tumours with some of the features of ccRCC they do not fully reproduce all of the characteristics of human ccRCC. A very recent study 15 showed that combined deletion of *Vhl* and *Pbrm1* causes renal cysts with subsequent development of ccRCCs after approximately 10 months, providing an autochthonous model that reflects the *VHL/PBRM1* mutant genetic subset of human ccRCC. In this study we identify another genetic combination that gives rise to ccRCC, furthering our understanding of the spectrum of molecular causes of this disease and providing an autochthonous mouse model to test new therapeutic strategies.

Results

Human ccRCCs exhibit recurrent copy number gains and losses of genes regulating p53 and the G1-S cell cycle checkpoint

To gain further insight into genetic changes that arise in ccRCC we utilised cBioPortal 16,17 to reanalyze genomic data from 448 sporadic ccRCCs from the TCGA dataset 10. We focused on alterations in the network of genes that regulate p53 and the G1-S cell cycle transition, including *TP53*, *MDM2*, *MDM4*, *CDK* inhibitor family genes, *RB* family genes, *CYCLIN*s and *CDK*s. While loss- or gain-of-function nucleotide level mutations in these genes occur rarely in ccRCC, copy number losses of negative regulators or gains of positive regulators of the network are common. 68% of human ccRCCs harbour a chromosomal copy

number alteration in at least one of these genes and most (78%) of these tumours harbour multiple simultaneous alterations (Supplementary Figure 1a). Patients with tumours that display alteration in at least one gene in the p53/G1-S network signature have a worse outcome than those without these genetic alterations (Supplementary Figure 1b). Alterations in other frequently mutated ccRCC genes including *VHL*, *PBRM1*, *BAP1* and *SETD2* are not enriched in the p53/G1-S network signature tumours (Supplementary Figure 1a), arguing that alterations of genes in this network arise independently of other putative mutational selection pressures during ccRCC evolution. These data give rise to the hypothesis that during the evolution of the majority of ccRCCs there is a selection for multiple copy number alterations that are predicted to alter the integrity of the G1/S cell cycle checkpoint, promoting tumour initiation and progression.

Vhl, *Trp53* and *Rb1* deletion allows the evolution of ccRCC in mice

To functionally test this idea in mice, we genetically deleted *Vhl* together with two tumour suppressor genes that encode proteins that function as the key controllers of cell cycle entry in the p53/G1-S network, namely *Trp53* (encoding p53) and *Rb1* (encoding pRB). We generated mice that allow inducible renal epithelial cell-specific (Ksp1.3-CreER^{T2}) 18 homozygous deletion of *loxP*-flanked alleles of *Rb1*, *Vhl/Rb1, Trp53/Rb1* and *Vhl/Trp53/Rb1* to complement our previous analyses of the effects of *Vhl* and *Vhl/Trp53* deletion 11,13. Epithelial cell-specific gene deletion throughout the nephron, including in proximal tubule epithelial cells 18, the likely cell of origin of ccRCC 19, was induced in pups by injecting nursing dams with tamoxifen or by feeding six week-old mice with tamoxifen-containing food. These two treatments yielded identical results and have been pooled for the purposes of the following descriptions. Hereafter $^{\Delta/\Delta}$ refers to deleted alleles. Littermate mice lacking the Ksp1.3-CreER^{T2} transgene served as wild type controls, denoted by $^{+/+}$. While p53 was not detectable by immunohistochemical staining, loss of immunoreactivity for pRB confirmed *Rb1* deletion in all genotypes and the nuclear accumulation of HIF-1α in Vhl$^{\Delta/\Delta}$Rb1$^{\Delta/\Delta}$ and Vhl$^{\Delta/\Delta}$Trp53$^{\Delta/\Delta}$Rb1$^{\Delta/\Delta}$ kidneys confirmed *Vhl* deletion (Supplementary Figure 2a). Kidneys of Rb1$^{\Delta/\Delta}$ (n=35 mice) and Vhl$^{\Delta/\Delta}$Rb1$^{\Delta/\Delta}$ (n=29 mice) mice displayed occasional sites of subtle disorganization of renal tubular epithelia 50-57 weeks after gene deletion (Figure 1a,b). Trp53$^{\Delta/\Delta}$Rb1$^{\Delta/\Delta}$ kidneys (n=12 mice) displayed small cysts (1-5 cysts per kidney section) (Figure 1c), as well as occasional sites of cystic or tubular dysplasia (Figure 1d,e) within 46-54 weeks of gene deletion. In contrast, within 30-47 weeks of gene deletion, 10 of 25 Vhl$^{\Delta/\Delta}$Trp53$^{\Delta/\Delta}$Rb1$^{\Delta/\Delta}$ mice developed a total of 64 tumours (Figure 1f-i). Mice that did not develop tumours showed an equivalent extent of tubular immunoreactivity for CA9 (Supplementary Figure 2b), a marker of *Vhl* deletion and HIF-α activation, to histologically normal tubules in kidneys with tumours, showing that the absence of tumours in these mice was not caused by failure of activation of Cre. The presence of apparent small precursor lesions in these mice (Supplementary Figure 2b) implies that tumours may potentially have developed at later timepoints. To follow up these observations in new cohorts of mice, we first established that the emergence of tumours in Vhl$^{\Delta/\Delta}$Trp53$^{\Delta/\Delta}$Rb1$^{\Delta/\Delta}$ mice could be monitored using contrast-assisted μCT imaging (Figure 1j) and followed tumour onset over time in larger cohorts of Trp53$^{\Delta/\Delta}$Rb1$^{\Delta/\Delta}$ and Vhl$^{\Delta/\Delta}$Trp53$^{\Delta/\Delta}$Rb1$^{\Delta/\Delta}$ mice (Figure 1k). 31 of 38 (82%) Vhl$^{\Delta/\Delta}$Trp53$^{\Delta/\Delta}$Rb1$^{\Delta/\Delta}$ mice fed tamoxifen at 6 weeks of age developed a total of 159

tumours within 25-61 weeks after tamoxifen treatment. In contrast, 6 of 25 (24%) $Trp53^{\Delta/\Delta}Rb1^{\Delta/\Delta}$ mice developed a total of 13 tumours within 50-70 weeks after tamoxifen. We conclude that *Vhl* deletion accelerates the onset and increases the incidence of tumour formation as well as increases the number of tumours per mouse. Interestingly, $Vhl^{\Delta/\Delta}Trp53^{\Delta/\Delta}Rb1^{\Delta/\Delta}$ male mice developed tumours at earlier timepoints and developed more tumours than female mice (Supplementary Figure 3a,b), consistent with the fact that human ccRCC is almost twice as likely to occur in males than females 20.

Based on the WHO 2016 criteria, all tumours in $Vhl^{\Delta/\Delta}Trp53^{\Delta/\Delta}Rb1^{\Delta/\Delta}$ mice were classified as grade 3 or grade 4 ccRCCs growing in either acinar, solid or pseudo-papillary growth patterns (Figure 1l-p). Some tumours exhibited a cystic component (Figure 1h, tumour 2). 60% of tumours contained cells with either completely optically clear cytoplasms (Figure 1l) or very weakly stained cytoplasms (Figure 1m). 28% of tumours exhibited more cytoplasmic eosin staining (Figure 1n) and resembled the eosinophilic variant of ccRCC. 5 tumours showed regions with obvious transitions between clear cell and eosinophilic morphology, arguing that these cytoplasmic appearances represent a continual phenotypic spectrum (Figure 1o). Indeed, similar eosinophilic cells can be found in high-grade human ccRCC or in hypoxic regions of ccRCC tumours. Regions of necrosis (data not shown) were observed in many of the mouse tumours and 2 tumours exhibited intratumoural haemorrhage (Figure 1h, tumour 3). Necrosis and haemorrhage are also common features of human ccRCC. Two clear cell tumours also showed papillary-like features that arise rarely in VHL patients (Figure 1p) but did not show features of the newly described clear cell papillary RCC entity. These tumours were also distinguished from true papillary renal cell carcinomas by the absence of a fibrovascular core and absence of CK7 staining (data not shown). Importantly, irrespective of cytoplasmic morphology, all tumours displayed a highly developed vascular network of CD31- and von Willebrand Factor-positive thin-walled blood vessels enveloping clusters of carcinoma cells in a pseudoalveolar fashion (Figure 1q-t). These sinusoidal vascular structures are a characteristic diagnostic feature of human ccRCC. All tumours were confined to the kidney and exhibited pushing rather than infiltrative margins (Figure 1u). There was no evidence of invasion into blood vessels, peri-renal fat or the renal pelvis. No metastases were observed in the lungs, liver, spleen, bones or brains of tumour-bearing mice (n=19). In contrast to the ccRCC tumours in $Vhl^{\Delta/\Delta}Trp53^{\Delta/\Delta}Rb1^{\Delta/\Delta}$ kidneys, the tumours that arose in $Trp53^{\Delta/\Delta}Rb1^{\Delta/\Delta}$ kidneys exhibited a range of non-ccRCC phenotypes and were variously characterised by sarcomatoid and rhabdoid tumour cell morphologies, eosinophilic cytoplasms, comedonecrosis, atypical giant tumour cells and aberrant mitoses. (Supplementary Figure 4).

As well as ccRCCs, $Vhl^{\Delta/\Delta}Trp53^{\Delta/\Delta}Rb1^{\Delta/\Delta}$ kidneys exhibited a spectrum of lesions (Supplementary Figure 5) that recapitulate the putative precursor lesions that are found in human VHL patient kidneys, namely cysts with a single epithelial layer, cysts with proliferation of atypical cells growing in multilayered structures in the cystic lumen, as well as small solid lesions that appear to have no cystic component. ccRCCs in this model therefore appear to arise via both cystic and solid precursor lesions.

Mouse ccRCCs are molecularly similar to human ccRCCs

Immunohistochemical stainings revealed numerous similarities between $Vhl^{\Delta/\Delta}Trp53^{\Delta/\Delta}Rb1^{\Delta/\Delta}$ mouse ccRCCs and human ccRCCs (Figure 2). All mouse ccRCCs displayed nuclear accumulation of HIF-2α (n=41) and 75% displayed nuclear accumulation of HIF-1α (n=47), consistent with the fact that while most human ccRCCs express both HIF-1α and HIF-2α, approximately 30% express only HIF-2α but not HIF-1αΔ21. All tumours stained positively for the HIF-α target CA9 (n=46). It is noteworthy that histologically normal tubules in $Vhl^{\Delta/\Delta}Trp53^{\Delta/\Delta}Rb1^{\Delta/\Delta}$ kidneys frequently exhibited HIF-1α, HIF-2α and CA9 immunoreactivity (Figure 2), demonstrating that these mutant cells had not become tumours within 9-11 months of gene deletion. All tumours showed strong staining for phospho-Thr37/46-4E-BP1 (n=44), indicative of strong mTORC1 activation, a common feature of human ccRCC. In contrast, antibodies against phospho-Thr202/Tyr204-ERK1/2, a marker of activation of the RAS-MAPK pathway, labelled only rare cells in most tumours (n=44). All tumours showed strong immunoreactivity for PAX8 (n=47) (Figure 2) and pan-cytokeratin (n=47) (Supplementary Figure 6), which are clinical diagnostic markers for ccRCC. 39 of 43 tumours stained positively for CD10, 37 of 43 stained positively for AQP1 and 14 of 43 stained positively for NAPI2A (Supplementary Figure 6). All tumours were positive for at least one of these proximal tubule marker proteins and no tumour (n=43) displayed immunoreactivity for markers of loops of Henle (THP), distal tubules (NCC) or collecting ducts (AQP2) (Supplementary Figure 6). We conclude that even though the Cre driver induces gene deletion widely throughout the nephron, $Vhl^{\Delta/\Delta}Trp53^{\Delta/\Delta}Rb1^{\Delta/\Delta}$ mouse ccRCCs arise from proximal tubule epithelial cells.

In contrast to tumours in $Vhl^{\Delta/\Delta}Trp53^{\Delta/\Delta}Rb1^{\Delta/\Delta}$ kidneys, which exhibited uniform positive staining of HIF-1α and CA9, tumours in $Trp53^{\Delta/\Delta}Rb1^{\Delta/\Delta}$ kidneys stained positively only in specific regions, often bordering on necrotic areas, which are typically hypoxic in most types of tumours (Supplementary Figure 4). 11 of 11 tumours were positive for the proximal tubule marker CD10, 2 of 11 for NAPI2A and 0 of 11 for THP, implicating the proximal tubule as the likely cell of origin (Supplementary Figure 4).

We next utilized RNA sequencing to compare global mRNA abundance between 6 mouse ccRCCs and 3 non-transgenic kidney cortices from littermate $Vhl^{fl/fl}Trp53^{fl/fl}Rb1^{fl/fl}$ mice. Multidimensional scaling analysis demonstrated a clear segregation of global gene expression profiles between normals and tumours (Supplementary Figure 7a,b) with 1852 genes significantly upregulated more than 2-fold and 2010 genes significantly downregulated more than 2-fold (Figure 3a, Supplementary Table 1). Of the human orthologues of these mouse ccRCC differentially expressed genes, 37% were also present in a list of differentially expressed genes identified by comparing 72 normal kidney and 533 human ccRCC samples (Figure 3b). Moreover, correlation analysis between human ccRCC and mouse ccRCC of the average expression values for all unique orthologous gene pairs revealed a strong correlation in global transcriptional profiles, in particular for those genes that are highly expressed (Figure 3c). These data demonstrate that there are strong transcriptional similarities between the mouse ccRCC model and human ccRCCs. Predominant transcriptional signatures in mouse ccRCCs included upregulation of a set of HIF-1α and HIF-2α target genes that we previously identified as being upregulated

following deletion of *Vhl* in primary renal epithelial cells 22 (Figure 3d), upregulation of numerous genes that regulate cell cycle progression, DNA replication and mitosis (Figure 3e) as well as upregulation of a set of genes that regulate immune responses and inflammation (Figure 3f). Global comparisons of mouse ccRCC mRNA expression with gene expression profiles of micro-dissected normal mouse nephron segments 23 revealed strong expression correlations of all tumours with S1 and S3 proximal tubule segments but not with other nephron segments (Figure 3g). These data strongly argue that the proximal tubule is the origin of ccRCCs in this model, consistent with similar gene expression correlation analyses of human ccRCC 19 and with our immunohistochemical stainings.

Mouse ccRCCs exhibit similar genetic mutational profiles to human ccRCCs

The observation that ccRCCs arise *in vivo* after a relatively long latency implies that additional mutational events likely accumulate to allow tumour formation. To identify such cooperating genetic alterations we conducted exome sequencing of DNA isolated from 7 mouse ccRCCs and normal liver tissue from these 6 mice. An average of $4.52 \pm 0.56 \times 10^7$ total reads were obtained per sample, giving mean target coverages of 56 ± 5 fold. Specific losses of sequencing coverage of the *loxP*-flanked regions of the *Vhl*, *Trp53* and *Rb1* genes confirmed that tumours are triply mutant for all three genes (Supplementary Figure 7c). Copy number variants in tumours were determined by comparing to matched liver samples. All tumours exhibited a normal autosomal karyotype without evidence of whole chromosome aneuploidy. Large regions of gain and loss were rare but a total of 55 regions of copy number variation were identified. We focused analyses on named genes that were present in the minimal overlapping chromosomal regions of gain or loss between different tumours or that were amplified (present in 4 or more copies) in individual tumours (Figure 4a and Supplementary Table 2). Notably, 2 tumours harboured amplifications (estimated copy numbers of 59 and 66) of the *Myc* oncogene (Figure 4a, Supplementary Figure 7d) and these tumours exhibited very high levels of *Myc* mRNA (Figure 3e). Copy number gains or amplifications of *MYC* occur in 8-15% of human ccRCC and are associated with poor patient survival 10,24,25 (Figure 4c). We identified regions of human-mouse synteny and investigated whether similar copy number variations arise in human ccRCCs. Interestingly, when human tumours exhibit copy number gains of genes that were gained in the mouse ccRCCs, or losses of genes that were lost in the mouse ccRCCs, they almost invariably (with the exception of the *DYNTL1* syntenic region) arise specifically in the p53/G1-S network set of human tumours (Figure 4b), arguing that the copy number alterations in the mouse model are non-random and that they may participate in the evolution and progression of a subset of ccRCC. Consistent with this notion, copy number gain of *SYCP1* in human ccRCC predicts poor patient survival (Figure 4c).

Single nucleotide variants (SNVs) and insertions and deletions (InDels) were identified in mouse ccRCCs versus matched liver. The most frequent SNVs were C>A/G>T transversions, C>T/G>A transitions and A>G/T>C transitions (Figure 5a). These three classes of mutations are also the most frequently occurring in human ccRCC 10 demonstrating that the mouse model reproduces the same classes of mutations that arise in human ccRCC. Mouse ccRCCs exhibited 161 ± 17 non-synonymous mutations per tumour and these were almost entirely attributable to SNVs rather than InDels (Figure 5b). Human

ccRCCs exhibit 50.6 ± 20.3 non-synonymous mutations per tumour (n=382, cBioPortal), suggesting that $Vhl^{\Delta/\Delta}Trp53^{\Delta/\Delta}Rb1^{\Delta/\Delta}$ mouse ccRCCs do not appear to harbour fewer mutations than the human counterparts, a limitation of some genetically engineered mouse tumour models 26. To narrow the search for potential truncal or clonal cooperating mutations, we focused further analyses on the set of truncating and frameshift mutations that were present at variant allele frequency (VAF) greater than or equal to 5% plus non-synonymous coding mutations that were present at high (>25%) VAF (Supplementary Table 3). While mutations of mouse orthologues of commonly mutated genes in human ccRCC, including *Pbrm1*, *Bap1* and *Setd2* were not observed in these tumours, gene set enrichment analysis demonstrated striking enrichment in genes associated with GO terms for Cell Projection Part ($P = 3.91 \times 10^{-14}$), Vesicle Mediated Transport ($P = 5.89 \times 10^{-11}$) and Microtubule Cytoskeleton ($P = 1.71 \times 10^{-9}$), amongst other related gene sets. Further inspection revealed the recurrence of mutations in genes that are involved in regulating the structure or function of the primary cilium. Each of the 7 tumours exhibited one or more mutations in 12 primary cilium-related genes (Figure 5c), including *Kif3a* and *Kif3b*, which encode components of the Kinesin-2 microtubule motor complex that is necessary for the generation of primary cilia. Genetic deletion of *Kif3a* cooperates with loss of *Vhl* or *Vhl/Trp53* to promote the formation of ccRCC precursor lesions in mice 12,27. 11 of 12 of the human orthologues of these genes are mutated in small percentages of human ccRCCs, and extending the list to include other known human ciliopathy genes and genes for which there is evidence for a function in primary cilium biology, we identified that 40% of human ccRCCs harbour one or more mutations in primary cilium-related genes (Supplementary Figure 8). Importantly, these mutations are largely mutually exclusive of one another, and of *PTEN* mutations. We have previously shown that *Pten* mutation cooperates with *Vhl* mutation to reduce the frequency of ciliated renal epithelial cells and induces renal cysts 11. Similar to human ccRCCs 28, all mouse ccRCCs exhibited a reduced frequency of ciliated tumour cells (Figure 5d). These data uncover a mutational convergence on primary cilium-related genes in mouse and human ccRCCs.

Therapeutic studies using the mouse ccRCC model

Having established many molecular similarities between mouse and human ccRCC, together with the demonstration that different mouse ccRCCs are genetically distinct from one another, we next asked whether this model is useful for pre-clinical therapeutic studies. Patients with metastatic ccRCC typically receive anti-angiogenic therapy in the form of receptor tyrosine kinase inhibitors such as Sunitinib. Up to 20% of tumours are refractory to these therapies and the majority of patients typically develop resistance within 1 year. Second line therapy often involves mTOR inhibition (eg. Everolimus), which confers a moderate increase in progression-free survival compared to placebo. We first mimicked this therapeutic regime by monitoring tumour initiation and progression in $Vhl^{\Delta/\Delta}Trp53^{\Delta/\Delta}Rb1^{\Delta/\Delta}$ mice using contrast-assisted μCT imaging and we initiated therapy once the largest tumour in each mouse reached a volume of approximately 20-70 mm^3 (Figure 6a,b). Of 19 independent tumours in 4 mice, 6 tumours grew at a rapid rate under Sunitinib treatment, 3 tumours regressed and 10 were stable with no or slow growth (Figure 6c). Of these latter tumours, 6 developed resistance within 2-3 weeks and grew rapidly. Second line therapy with Everolimus showed stable disease or regression in 18 of 23

tumours (several new tumours developed during Sunitinib therapy), 4 of which developed resistance (Figure 6c). Thus, individual ccRCCs in $Vhl^{\Delta/\Delta}Trp53^{\Delta/\Delta}Rb1^{\Delta/\Delta}$ mice are differently sensitive to clinical agents used to treat human ccRCC, further validating the accuracy of the mouse model and suggesting that this model will be useful to interrogate mechanisms or identify biomarkers that are associated with therapeutic sensitivity or resistance.

Acriflavine, a drug that was given orally as a urinary antiseptic in the 1920s, was recently identified to inhibit the dimerization of HIF-1α and HIF-2α with HIF-1β, blocking transcriptional activation 29. Acriflavine treatment was shown to reduce the growth of various cancer cell lines in xenograft assays and reduce colorectal cancer growth in an autochthononous mouse model 29,30. Given the important pathogenic role of dysregulated HIF-α activity in human ccRCC we tested Acriflavine in the above-described mice as third line therapy after Sunitinib and Everolimus. Daily intraperitoneal injection slowed growth of 2 of 23 tumours and one large tumour that was resistant to Everolimus showed an initial regression but developed resistance after 3 weeks of Acriflavine therapy (Figure 6b,c). 3 smaller tumours regressed during Acriflavine therapy, while other similarly sized tumours in the same mice increased in size (Figure 6c, Supplementary Figure 9). While these proof-of-principle studies identified that this drug is effective in only a subset of tumours, these results provide further pre-clinical evidence to support the ongoing development and clinical testing of various HIF-α inhibitors with better specificities and pharmacological properties as therapies for ccRCC. This mouse model represents an experimental platform that should assist in the identification of biomarkers that could be used to predict which human ccRCC tumours are likely to respond to HIFα-inhibition.

Discussion

This study describes an autochthonous mouse model of ccRCC that accurately recapitulates the cellular and molecular features of human ccRCC. While the exact combination of biallelic inactivation of *VHL*, *TP53* and *RB1* is not common in human ccRCC tumours, $Vhl^{\Delta/\Delta}Trp53^{\Delta/\Delta}Rb1^{\Delta/\Delta}$ mice represent a genetic background that models the predicted effects of the many combinatorial gene copy number alterations in regulators of the interconnected networks governing the p53 pathway and the G1-S cell cycle control machinery that arise in human ccRCC. The $Vhl^{\Delta/\Delta}Trp53^{\Delta/\Delta}Rb1^{\Delta/\Delta}$ genetic background does not automatically confer tumour-forming capacity on renal epithelial cells *in vivo* but rather permits the evolution of genetically distinct ccRCC tumours. The dependency of these tumours on *Vhl* mutation is clearly shown by the accelerated and increased incidence of tumour formation in $Vhl^{\Delta/\Delta}Trp53^{\Delta/\Delta}Rb1^{\Delta/\Delta}$ mice compared to $Trp53^{\Delta/\Delta}Rb1^{\Delta/\Delta}$ mice, as well as the fact that only $Vhl^{\Delta/\Delta}Trp53^{\Delta/\Delta}Rb1^{\Delta/\Delta}$ mice develop ccRCCs. These functional genetic data are consistent with the fact that *VHL* is biallelically inactivated as an initiating event in the vast majority of ccRCCs 6,7,10. We identified a mutational convergence on genes that regulate the structure or function of the primary cilium in mouse ccRCCs and in 40% of human ccRCCs. Due to their individual relative rarity, these mutations had been previously missed by statistical analyses to identify recurrent mutations but when considered in the larger biological context we propose that at least a subset of ccRCC can be viewed as genetic ciliopathies. While further functional studies will be necessary to establish whether

the mutations that we identified in ccRCC play a pathogenic role in the disease, given that a common phenotypic outcome of genetic alterations in diverse genes that are important for cilia biology is the induction of renal epithelial cell proliferation and cyst formation 31, it appears likely that primary cilium gene mutations might either permit or enhance the proliferation of *VHL* mutant cells. In this context, our previous studies have shown cooperation between loss of *Vhl* and loss of primary cilia in causing uncontrolled renal epithelial proliferation and development of simple and atypical cystic precursor lesions in mice 11,12,27,32. It is plausible that the combination of *VHL* mutation, primary cilium gene mutation and additional genetic alterations, such as in the p53 and G1-S cell cycle network or in other frequently mutated tumour suppressor genes like *PBRM1*, *BAP1* or *SETD2*, act cooperatively to cause the evolution of ccRCC. It is noteworthy that none of the 7 mouse ccRCCs examined in this study showed mutations in these tumour suppressor genes, arguing that this model may reflect the approximately 50% of ccRCCs that do not harbour mutations in other known or suspected kidney cancer tumour suppressor genes.

The $Vhl^{\Delta/\Delta}Trp53^{\Delta/\Delta}Rb1^{\Delta/\Delta}$ mouse ccRCC model will provide an opportunity to assess genetic dependencies and identify mutational modifiers that enhance tumour initiation or promote invasion and metastasis. Our gene copy number analyses identified several candidate genes, including the *Myc* oncogene and *Loxl2*, which have been implicated in various aspects of the pathogenesis of ccRCC 21,33–36. It is also noteworthy that all $Vhl^{\Delta/\Delta}Trp53^{\Delta/\Delta}Rb1^{\Delta/\Delta}$ mouse ccRCCs showed high levels of mTORC1 activation, as evidenced by phospho-Thr37/46-4E-BP1 staining. PI3K-mTORC1 pathway activation was also observed in cysts or tumours in *Vhl/Pten* 11, *Vhl/Trp53* 13, *Vhl/Trp53/Kif3a* 27, *Vhl/Bap1* 14 and *Vhl/Pbrm1* 15 mutant mice, suggesting that PI3K-mTORC1 pathway activation might generally promote ccRCC evolution in the context of diverse cooperating mutations.

The fact that different $Vhl^{\Delta/\Delta}Trp53^{\Delta/\Delta}Rb1^{\Delta/\Delta}$ ccRCCs are genetically distinct from one another, coupled with our observations that different ccRCCs within and between mice responded differently to therapeutic regimes used to treat human metastatic ccRCC, suggests that this experimental system will be useful for the identification of molecular determinants of tumour sensitivities and resistances. Our observations of therapeutic effects of the HIF-1α and HIF-2α inhibitor Acriflavine on at least some tumours support recent findings that a new HIF-2α-specific inhibitor shows good therapeutic activity in various pre-clinical models towards approximately half of human ccRCC tumour-derived cell lines or tumourgrafts 37,38. Finally, the availability of this and other autochthonous models of ccRCC will allow investigations of the role of the tumour microenvironment in tumour progression and therapeutic responses, particularly in the context of the ongoing optimisation of immune checkpoint-blocking therapies, which have already yielded good clinical responses in sub-fractions of ccRCC patients 39.

Online Methods

Mice

$Rb1^{fl/fl}$ (FVB;129P2 background) 40, $Vhl^{fl/fl}$ (C;129S background) 41 and $Trp53^{fl/fl}$ (FVB;129P2 background) 42 mice were crossed with Ksp1.3-$CreER^{T2}$ (B6.Cg background) 18 mice to generate Ksp1.3-$CreER^{T2}$;$Vhl^{fl/fl}$;$Trp53^{fl/fl}$;$Rb1^{fl/fl}$, Ksp1.3-

CreER^{T2};*Vhl*$^{fl/fl}$;*Rb1*$^{fl/fl}$, Ksp1.3-CreER^{T2};*Trp53*$^{fl/fl}$;*Rb1*$^{fl/fl}$ and Ksp1.3-CreER$^{T2\ Tg/+}$;*Rb1*$^{fl/fl}$ animals. Littermate mice that lacked the Cre transgene served as wild type controls. Gene deletion in 6 week-old mice was achieved by feeding with food containing tamoxifen (400 parts per million) for 2 weeks. For gene deletion in pups, nursing dams were injected intraperitoneally with tamoxifen (0.1 mg/g body weight) from days P2–P4. Mouse crosses and phenotyping were conducted under the breeding license of the Laboratory Animal Services Center, University of Zurich and tumour monitoring studies were conducted under license ZH116/16 of the Canton of Zurich. Investigators were not blinded to the genotype of the mice.

Immunohistochemistry and immunofluorescence

Immunohistochemistry and immunofluorescence were conducted using previously described methods 11 using the antibodies against the following antigens AQP1 (Abcam, ab15080), AQP2 (gift from Johannes Loffing, 43), CA9 (Invitrogen, PA1-16592), CD10 (Thermo Fisher Scientific PA5-47075), CD31 (Abcam, ab28364), pan-Cytokeratin (DAKO, M3515), HIF-1α (Novus Biotechnologies, NB-100-105), HIF-2α (PM8, gift from Patrick Pollard, 44), NAPI2A (gift from Jürg Biber, 45), NCC (Millipore, AB3553), PAX8 (Protein Tech Group, 10336-1-AP), Phospho-Thr202/Tyr204-Erk1/2 (Cell Signaling Technologies, 9101), Phospho-Thr37/46-4E-BP1 (Cell Signaling Technologies, 2855), pRB (BD Biosciences, 554136), THP (Santa Cruz Biotechnologies, SC-20631), acetylated-Tubulin (Sigma-Aldrich, T6793), vWF (Sigma, F3520).

Therapeutic studies and μCT imaging

Imaging of animals was performed as previously described 12. Mice were imaged monthly beginning 5 months after tamoxifen feeding and every week or every two weeks during therapeutic studies. Tumour volumes were determined from μCT images by measuring the maximum diameter of tumours in the x, y and z planes and using the formula for the volume of an ellipsoid ($V = 4/3 \times \pi \times radius_x \times radius_y \times radius_z$). As a first line therapy animals with tumours between 20-70 mm^3 received 40 mg/kg Sunitinib (dissolved in 0.5% carboxy-methyl-cellulose, 5% dextrose) every day via oral gavage. If tumours did not respond or developed resistance to Sunitinib, therapy was switched to daily 10 mg/kg Everolimus (dissolved in 5% PEG, 5% Tween80, 5% EtOH and 85% D5W) via oral gavage. As a third line therapy 2 mg/kg Acriflavine dissolved in PBS was injected intraperitoneally every day.

RNA sequencing

RNA isolated from 6 ccRCCs from Vhl$^{\Delta/\Delta}$Trp53$^{\Delta/\Delta}$Rb1$^{\Delta/\Delta}$ mice (2 tumours were from the same mouse) and from renal cortex samples from 3 non-transgenic Vhl$^{fl/fl}$Trp53$^{fl/fl}$Rb1$^{fl/fl}$ littermate mice was subjected to RNA sequencing by Otogenetics Corporation (USA). Starting from the raw .fastq files (2x150bp) the reads were mapped against the mouse reference genome GRCm38 (with ENSEMBL annotation GRCm38.p4, release 84) using the STAR aligner (version 2.4.2a) 46. Standard quality control (*Picard* and *RSeQC*) 47 was run to assess the quality of the resulting alignments. Subsequently, strand-specific (reversely stranded) read counting was performed using *featureCount* (subread, version 1.5.0) 48 yielding count tables for 47729 transcripts per sample. Between 1.9-3.8x10^7 mapped reads were obtained per sample. To avoid technical artifacts the data were filtered such that genes

where the average over all samples was less than 5 counts were removed. This resulted in 29111 transcripts removed out of 47729 in total, leaving 18618 transcripts for further analysis. Differential expression was modelled using generalized linear regression of the negative binomial family, as implemented in the R-package *DESeq2* 49. TCGA RNASeqV2 mRNA data for human ccRCC and normal kidneys were downloaded using the *TCGA2STAT* package. *Limma/voom* 50 was used to identify differentially expressed genes in this data set. Comparisons were made using only mouse and human genes with one-to-one orthology. Similarity to normal nephron segment expression profiles was assessed following the described procedure of Davis *et al.* 19. Briefly, the Pearson correlation coefficients between each mouse tumor sample and the nephron segment specific reference data sets were calculated over all common genes 23. Independently, competitive enrichment of nephron segment-specific gene sets was performed using Fisher's exact test. The negative logarithmic p-value can serve as a similarity score and gave results analogous to the Pearson coefficient. Global similarities in gene expression between mouse and human ccRCC were determined using Pearson correlation analysis of the normalised log-transformed gene expression values for all unique orthologous gene pairs in human (RNA sequencing data from TCGA studies) and mouse (this study) ccRCCs.

Exome sequencing

Genomic DNA isolated from 7 ccRCCs from $Vhl^{\Delta/\Delta}Trp53^{\Delta/\Delta}Rb1^{\Delta/\Delta}$ mice (2 tumours were from the same mouse), from 6 normal liver samples from the tumour-bearing mice and from renal cortex samples from 3 wild type mice was subjected to exome sequencing by Otogenetics Corporation (USA) using Agilent's SureSelect Mouse All Exon V1 kit. The raw fastq files were mapped against the mouse reference (GRCm38/mm10) using *bwa mem* (http://github.com/lh3/bwa). Subsequently, Picard tools *MarkDuplicates* and GATK *IndelRealigner* 51 were used to improve the final alignments. Picard tools *AlignmentSummaryMetrics* and *HsMetrics* were used to perform quality control on the raw sequencing data and the alignments. Somatic SNVs were called for each tumor-normal combination using two tools: *mutect* and *strelka*. Small somatic InDels were called using *strelka*. Merging and filtering of variant calls was performed using GATK 51 and only variants with variant allele frequencies greater than 5% were included in the analyses. *SnpEff* 52, *SnpSift* 53 and *BEDTools* 54 were used for annotations. *EXCAVATOR* 55 was used to call copy number variations with 95% probability cut-off in tumours against the matched normal liver samples. Lists of copy number variants were manually filtered to remove calls in which multiple tumours showed the exact start and end points of the gain or loss, as these are highly likely to represent artefacts of the calling algorithm. Result files were annotated with mouse and human genes using *BEDTools* 54. We used the non-mouse refgenes track (xenoRefGene) from the UCSC Genome Browser 56 (http://genome.ucsc.edu/) to map human genes to the mouse genome. Gene set enrichment analysis was conducted using the online GSEA software (http://software.broadinstitute.org/gsea/index.jsp).

Survival analyses

Human ccRCC Kaplan-Meier survival analyses were conducted using the online tools of the cBioPortal for Cancer Genomics (http://www.cbioportal.org).

Statistics

All sample size (n) values used for statistical analyses are provided in the relevant figures and supplementary figures. Differences in tumour onset between different mouse genotypes and sexes were assessed using the Log-rank Mantel-Cox test and differences in tumour numbers between mice were assessed using Student's one-tailed unpaired t-test. Pearson correlation analyses were used to compare global mouse and human ccRCC mRNA expression as well as to compare mouse ccRCC mRNA expression with nephron segment-specific mRNA expression profiles.

Data availability

Exome sequencing or RNA sequencing datasets (beyond the summaries that are deposited as Supplementary Information) are available from the corresponding author upon reasonable request.

Supplementary Material

Refer to Web version on PubMed Central for supplementary material.

Acknowledgements

This work was supported by grants to IJF from Swiss National Science Foundation (PP00P3_128257), European Research Council (260316) and VHL Family Alliance.

References

1. Hsieh JJ, et al. Renal cell carcinoma. Nature Publishing Group. 2017; 3:17009.
2. Ghatalia P, Zibelman M, Geynisman DM, Plimack ER. Checkpoint Inhibitors for the Treatment of Renal Cell Carcinoma. 2017; :1–14. DOI: 10.1007/s11864-017-0458-0
3. Choueiri TK, Motzer RJ. Systemic Therapy for Metastatic Renal-Cell Carcinoma. The New England journal of medicine. 2017; 376:354–366. [PubMed: 28121507]
4. Moore LE, et al. Von Hippel-Lindau (VHL) inactivation in sporadic clear cell renal cancer: associations with germline VHL polymorphisms and etiologic risk factors. PLoS Genet. 2011; 7:e1002312. [PubMed: 22022277]
5. Nickerson ML, et al. Improved identification of von Hippel-Lindau gene alterations in clear cell renal tumors. Clinical cancer research : an official journal of the American Association for Cancer Research. 2008; 14:4726–4734. [PubMed: 18676741]
6. Sato Y, et al. Integrated molecular analysis of clear-cell renal cell carcinoma. Nature genetics. 2013; 45:860–867. [PubMed: 23797736]
7. Gerlinger M, et al. Genomic architecture and evolution of clear cell renal cell carcinomas defined by multiregion sequencing. Nature genetics. 2014; 46:225–233. [PubMed: 24487277]
8. Mandriota SJ, et al. HIF activation identifies early lesions in VHL kidneys: evidence for site-specific tumor suppressor function in the nephron. Cancer cell. 2002; 1:459–468. [PubMed: 12124175]
9. Frew IJ, Moch H. A clearer view of the molecular complexity of clear cell renal cell carcinoma. Annu Rev Pathol. 2015; 10:263–289. [PubMed: 25387056]
10. Cancer Genome Atlas Research Network. Comprehensive molecular characterization of clear cell renal cell carcinoma. Nature. 2013; 499:43–49. [PubMed: 23792563]
11. Frew IJ, et al. pVHL and PTEN tumour suppressor proteins cooperatively suppress kidney cyst formation. EMBO J. 2008; 27:1747–1757. [PubMed: 18497742]

12. Lehmann H, Vicari D, Wild PJ, Frew IJ. Combined Deletion of Vhl and Kif3a Accelerates Renal Cyst Formation. Journal of the American Society of Nephrology. 2015; 26:2778–2788. [PubMed: 25788526]
13. Albers J, et al. Combined mutation of Vhl and Trp53 causes renal cysts and tumours in mice. EMBO Mol Med. 2013; 5:949–964. [PubMed: 23606570]
14. Wang S-S, et al. Bap1 is essential for kidney function and cooperates with Vhl in renal tumorigenesis. Proceedings of the National Academy of Sciences. 2014; 111:16538–16543.
15. Nargund AM, et al. The SWI/SNF Protein PBRM1 Restrains VHL-Loss-Driven Clear Cell Renal Cell Carcinoma. CellReports. 2017; 18:2893–2906.
16. Gao J, et al. Integrative analysis of complex cancer genomics and clinical profiles using the cBioPortal. Sci Signal. 2013; 6:pl1. [PubMed: 23550210]
17. Cerami E, et al. The cBio cancer genomics portal: an open platform for exploring multidimensional cancer genomics data. Cancer Discov. 2012; 2:401–404. [PubMed: 22588877]
18. Patel V, et al. Acute kidney injury and aberrant planar cell polarity induce cyst formation in mice lacking renal cilia. Human molecular genetics. 2008; 17:1578–1590. [PubMed: 18263895]
19. Davis CF, et al. The somatic genomic landscape of chromophobe renal cell carcinoma. Cancer cell. 2014; 26:319–330. [PubMed: 25155756]
20. Ricketts CJ, Linehan WM. Gender Specific Mutation Incidence and Survival Associations in Clear Cell Renal Cell Carcinoma (CCRCC). PloS one. 2015; 10:e0140257. [PubMed: 26484545]
21. Gordan JD, et al. HIF-alpha effects on c-Myc distinguish two subtypes of sporadic VHL-deficient clear cell renal carcinoma. Cancer cell. 2008; 14:435–446. [PubMed: 19061835]
22. Schönenberger D, et al. Formation of Renal Cysts and Tumors in Vhl/Trp53-Deficient Mice Requires HIF1α and HIF2α. Cancer Research. 2016; 76:2025–2036. [PubMed: 26759234]
23. Cheval L, Pierrat F, Rajerison R, Piquemal D, Doucet A. Of mice and men: divergence of gene expression patterns in kidney. PloS one. 2012; 7:e46876. [PubMed: 23056504]
24. Klatte T, et al. Gain of chromosome 8q is associated with metastases and poor survival of patients with clear cell renal cell carcinoma. Cancer. 2012; 118:5777–5782. [PubMed: 22605478]
25. Beroukhim R, et al. Patterns of gene expression and copy-number alterations in von-hippel lindau disease-associated and sporadic clear cell carcinoma of the kidney. Cancer research. 2009; 69:4674–4681. [PubMed: 19470766]
26. Westcott PMK, et al. The mutational landscapes of genetic and chemical models of Kras-driven lung cancer. Nature. 2015; 517:489–492. [PubMed: 25363767]
27. Guinot A, Lehmann H, Wild PJ, Frew IJ. Combined deletion of Vhl, Trp53 and Kif3a causes cystic and neoplastic renal lesions. The Journal of pathology. 2016; 239:365–373. [PubMed: 27126173]
28. Schraml P, et al. Sporadic clear cell renal cell carcinoma but not the papillary type is characterized by severely reduced frequency of primary cilia. Mod Pathol. 2009; 22:31–36. [PubMed: 18660794]
29. Lee K, et al. Acriflavine inhibits HIF-1 dimerization, tumor growth, and vascularization. Proceedings of the National Academy of Sciences. 2009; 106:17910–17915.
30. Shay JES, et al. Inhibition of hypoxia-inducible factors limits tumor progression in a mouse model of colorectal cancer. Carcinogenesis. 2014; 35:1067–1077. [PubMed: 24408928]
31. Pan J, Seeger-Nukpezah T, Golemis EA. The role of the cilium in normal and abnormal cell cycles: emphasis on renal cystic pathologies. Cell Mol Life Sci. 2013; 70:1849–1874. [PubMed: 22782110]
32. Thoma CR, et al. pVHL and GSK3beta are components of a primary cilium-maintenance signalling network. Nat Cell Biol. 2007; 9:588–595. [PubMed: 17450132]
33. Gordan JD, Thompson CB, Simon MC. HIF and c-Myc: sibling rivals for control of cancer cell metabolism and proliferation. Cancer cell. 2007; 12:108–113. [PubMed: 17692803]
34. Hase H, et al. LOXL2 status correlates with tumor stage and regulates integrin levels to promote tumor progression in ccRCC. Molecular Cancer Research. 2014; 12:1807–1817. [PubMed: 25092917]

35. Nishikawa R, et al. Tumour-suppressive microRNA-29s directly regulate LOXL2 expression and inhibit cancer cell migration and invasion in renal cell carcinoma. FEBS letters. 2015; 589:2136–2145. [PubMed: 26096783]
36. Kurozumi A, et al. Regulation of the collagen cross-linking enzymes LOXL2 and PLOD2 by tumor-suppressive microRNA-26a/b in renal cell carcinoma. Int J Oncol. 2016; 48:1837–1846. [PubMed: 26983694]
37. Cho H, et al. On-target efficacy of a HIF-2α antagonist in preclinical kidney cancer models. Nature. 2016; 539:107–111. [PubMed: 27595393]
38. Chen W, et al. Targeting renal cell carcinoma with a HIF-2 antagonist. Nature. 2016; 539:112–117. [PubMed: 27595394]
39. Motzer RJ, et al. Nivolumab versus Everolimus in Advanced Renal-Cell Carcinoma. The New England journal of medicine. 2015; 373:1803–1813. [PubMed: 26406148]
40. Marino S, Vooijs M, van Der Gulden H, Jonkers J, Berns A. Induction of medulloblastomas in p53-null mutant mice by somatic inactivation of Rb in the external granular layer cells of the cerebellum. Genes & development. 2000; 14:994–1004. [PubMed: 10783170]
41. Haase VH, Glickman JN, Socolovsky M, Jaenisch R. Vascular tumors in livers with targeted inactivation of the von Hippel-Lindau tumor suppressor. Proc Natl Acad Sci USA. 2001; 98:1583–1588. [PubMed: 11171994]
42. Jonkers J, et al. Synergistic tumor suppressor activity of BRCA2 and p53 in a conditional mouse model for breast cancer. Nature genetics. 2001; 29:418–425. [PubMed: 11694875]
43. Wagner CA, et al. Mouse model of type II Bartter's syndrome. II. Altered expression of renal sodium- and water-transporting proteins. Am J Physiol Renal Physiol. 2008; 294:F1373–80. [PubMed: 18322017]
44. Pollard PJ, et al. Targeted inactivation of fh1 causes proliferative renal cyst development and activation of the hypoxia pathway. Cancer cell. 2007; 11:311–319. [PubMed: 17418408]
45. Custer M, Lotscher M, Biber J, Murer H, Kaissling B. Expression of Na-P(i) cotransport in rat kidney: localization by RT-PCR and immunohistochemistry. The American journal of physiology. 1994; 266:F767–74. [PubMed: 7515582]
46. Dobin A, et al. STAR: ultrafast universal RNA-seq aligner. Bioinformatics. 2012
47. Wang L, et al. RSeQC: Quality Control of RNA-seq experiments. Bioinformatics. 2012
48. Liao Y, et al. featureCounts: an efficient general purpose program for assigning sequence reads to genomic features. Bioinformatics. 2014; 30:923–930. [PubMed: 24227677]
49. Love MI, Huber W, Anders S. Moderated estimation of fold change and dispersion for RNA-seq data with DESeq2. Genome Biol. 2014; 15:550. [PubMed: 25516281]
50. Ritchie ME, et al. limma powers differential expression analyses for RNA-sequencing and microarray studies. Nucleic acids research. 2015; 43:e47. [PubMed: 25605792]
51. McKenna A, et al. The Genome Analysis Toolkit: A MapReduce framework for analyzing next-generation DNA sequencing data. Genome Res. 2010; 20:1297–1303. [PubMed: 20644199]
52. Cingolani P, et al. A program for annotating and predicting the effects of single nucleotide polymorphisms, SnpEff: SNPs in the genome of Drosophila melanogaster strain w(1118); iso-2; iso-3. Fly. 2012; 6:80–92. [PubMed: 22728672]
53. Cingolani P, et al. Using Drosophila melanogaster as a Model for Genotoxic Chemical Mutational Studies with a New Program, SnpSift. Front Gene. 2012; 3
54. Quinlan AR, Hall IM. BEDTools: a flexible suite of utilities for comparing genomic features. Bioinformatics. 2010; 26:841–842. [PubMed: 20110278]
55. Magi A, et al. EXCAVATOR: detecting copy number variants from whole-exome sequencing data. Genome Biol. 2013; 14:R120. [PubMed: 24172663]
56. Rosenbloom KR, et al. The UCSC Genome Browser database: 2015 update. Nucleic acids research. 2015; 43:D670–D681. [PubMed: 25428374]

Europe PMC Funders Author Manuscripts

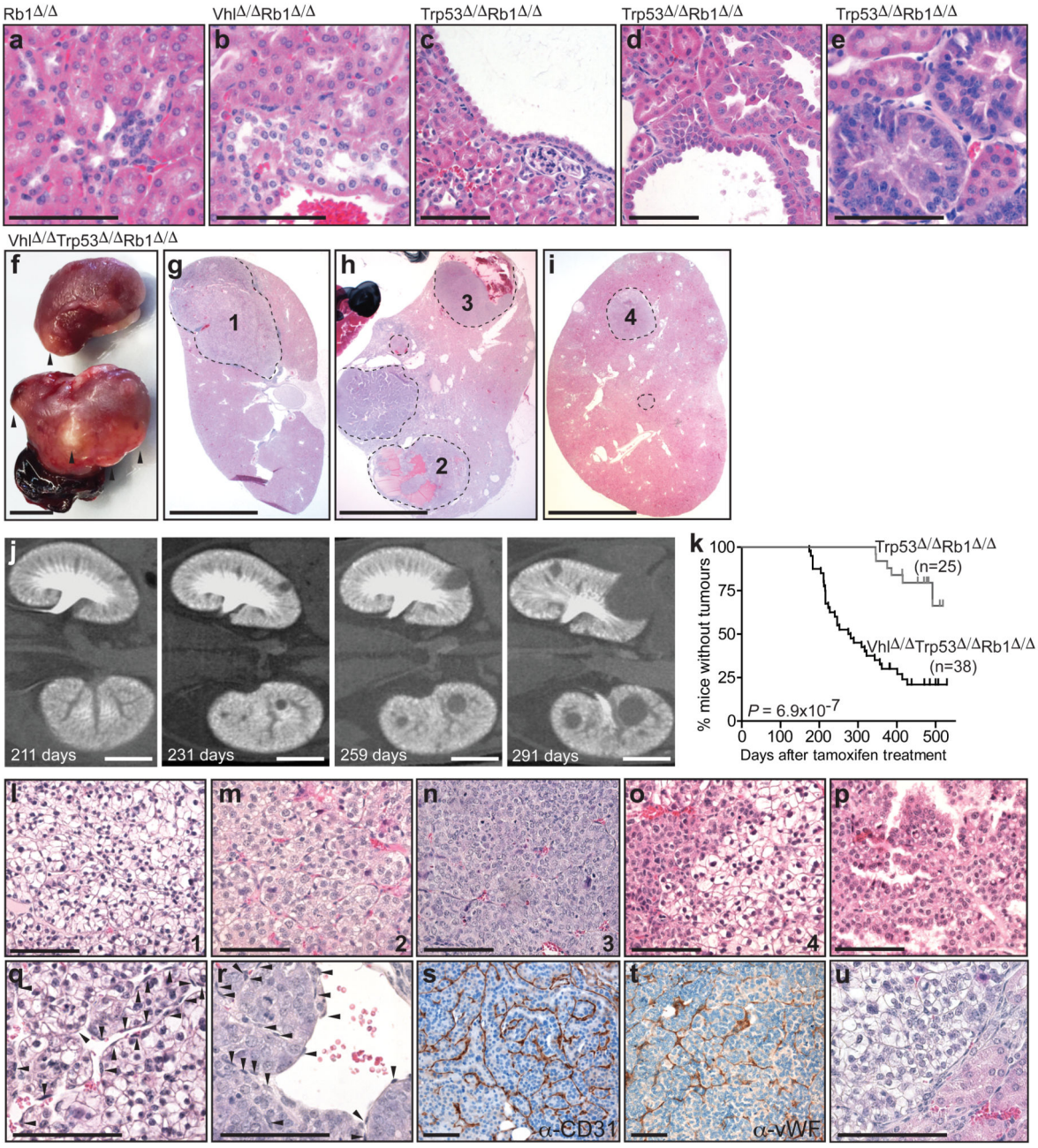

Figure 1. Renal epithelial cell-specific deletion of *Vhl/Trp53/Rb1* permits the evolution of ccRCCs

(**a,b**) Examples of mild renal tubular disorganization in 12 month-old (**a**) $Rb1^{\Delta/\Delta}$ mouse and (**b**) $Vhl^{\Delta/\Delta}Rb1^{\Delta/\Delta}$ mouse. (**c-e**) Examples of (**c**) simple cyst, (**d**) dysplasia associated with cysts and (**e**) solid dysplasia in a 12 month-old $Trp53^{\Delta/\Delta}Rb1^{\Delta/\Delta}$ mouse. (**f**) Kidneys from a 10 month-old $Vhl^{\Delta/\Delta}Trp53^{\Delta/\Delta}Rb1^{\Delta/\Delta}$ mouse. (**g-i**) Examples of histological sections of 10 month-old $Vhl^{\Delta/\Delta}Trp53^{\Delta/\Delta}Rb1^{\Delta/\Delta}$ mice with tumours outlined with dotted lines. (**j**) Example of longitudinal μCT imaging of tumour development in a $Vhl^{\Delta/\Delta}Trp53^{\Delta/\Delta}Rb1^{\Delta/\Delta}$ mouse, timepoints are days post tamoxifen feeding. (**k**) Tumour onset in cohorts of

$Vhl^{\Delta/\Delta}Trp53^{\Delta/\Delta}Rb1^{\Delta/\Delta}$ and $Trp53^{\Delta/\Delta}Rb1^{\Delta/\Delta}$ mice. *P* value is from the Log-rank Mantel-Cox test (**l-o**) Histological appearances of tumours 1-4 from **g-i** respectively, (**l**) pure clear cell cystoplasm, (**m**) clear cell cytoplasm with weak eosinophilic staining (**n**) strong cytoplasmic eosinophilic staining, (**o**) mixture of clear cell and eosinophilic cytoplasms. (**p**) Example of a papillary-like ccRCC. (**q-t**) Sinusoidal vascular networks in a tumour with (**q**) clear cell appearance and (**r**) eosinophilic appearance with endothelial cells highlighted by arrowheads. (**s**) CD31 and (**t**) von Willebrand Factor immunohistochemical stainings in ccRCCs from $Vhl^{\Delta/\Delta}Trp53^{\Delta/\Delta}Rb1^{\Delta/\Delta}$ mice. (**u**) Example of a tumour margin of a mouse ccRCC. Scale bars in a-e, l-u = 50 μm, scale bars in f-j = 5 mm.

Europe PMC Funders Author Manuscripts

Europe PMC Funders Author Manuscripts

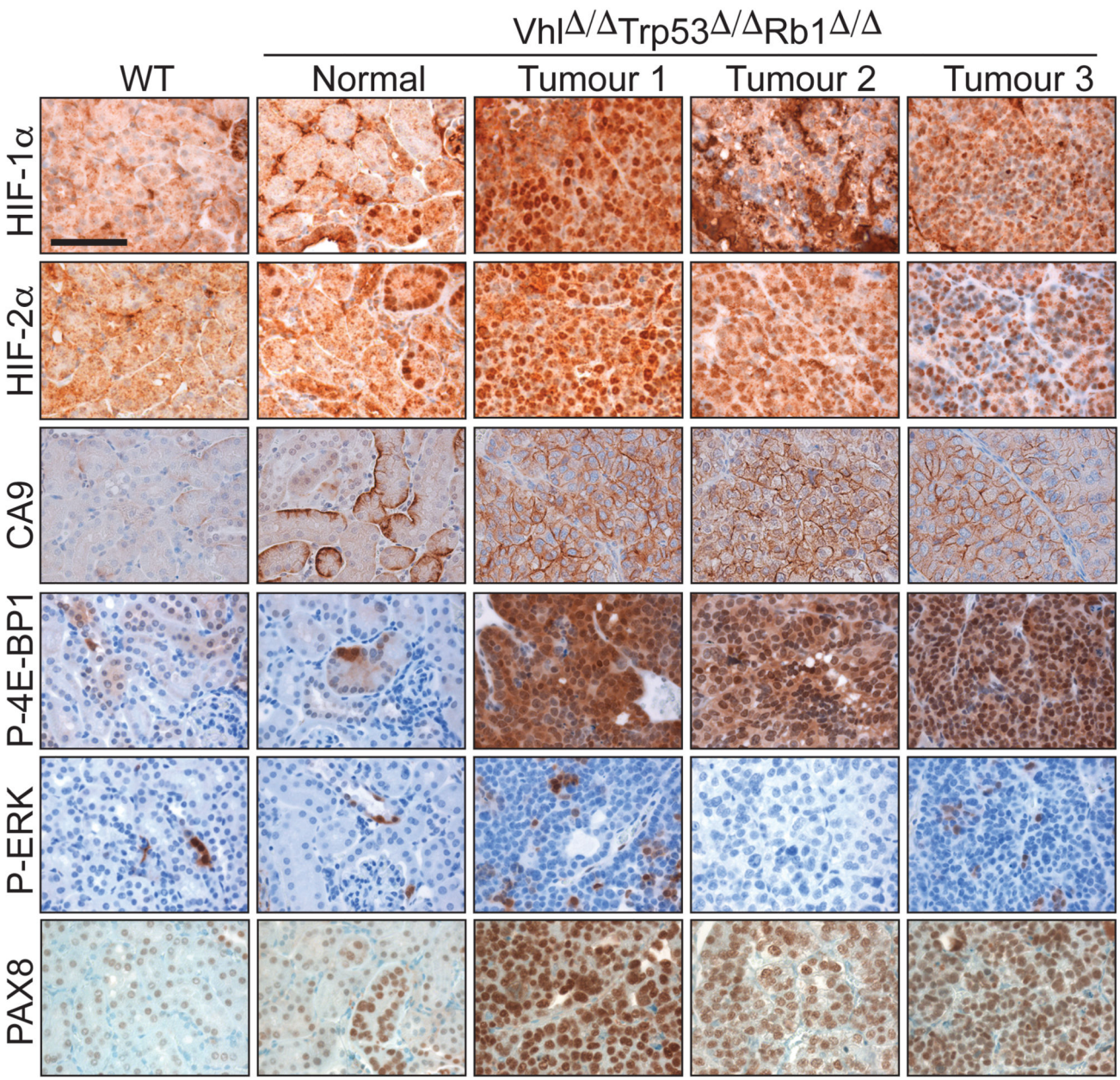

Figure 2. ccRCCs in Vhl$^{\Delta/\Delta}$Trp53$^{\Delta/\Delta}$Rb1$^{\Delta/\Delta}$ mice exhibit HIF-α and mTORC1 pathway activation

Examples of immunohistochemical stainings using antibodies against the indicated proteins in normal kidney tissue from a wild type mouse, histologically normal tissue from a tumour-bearing Vhl$^{\Delta/\Delta}$Trp53$^{\Delta/\Delta}$Rb1$^{\Delta/\Delta}$ mouse and three ccRCCs from Vhl$^{\Delta/\Delta}$Trp53$^{\Delta/\Delta}$Rb1$^{\Delta/\Delta}$ mice. All panels are the same magnification, scale bar = 50 μm.

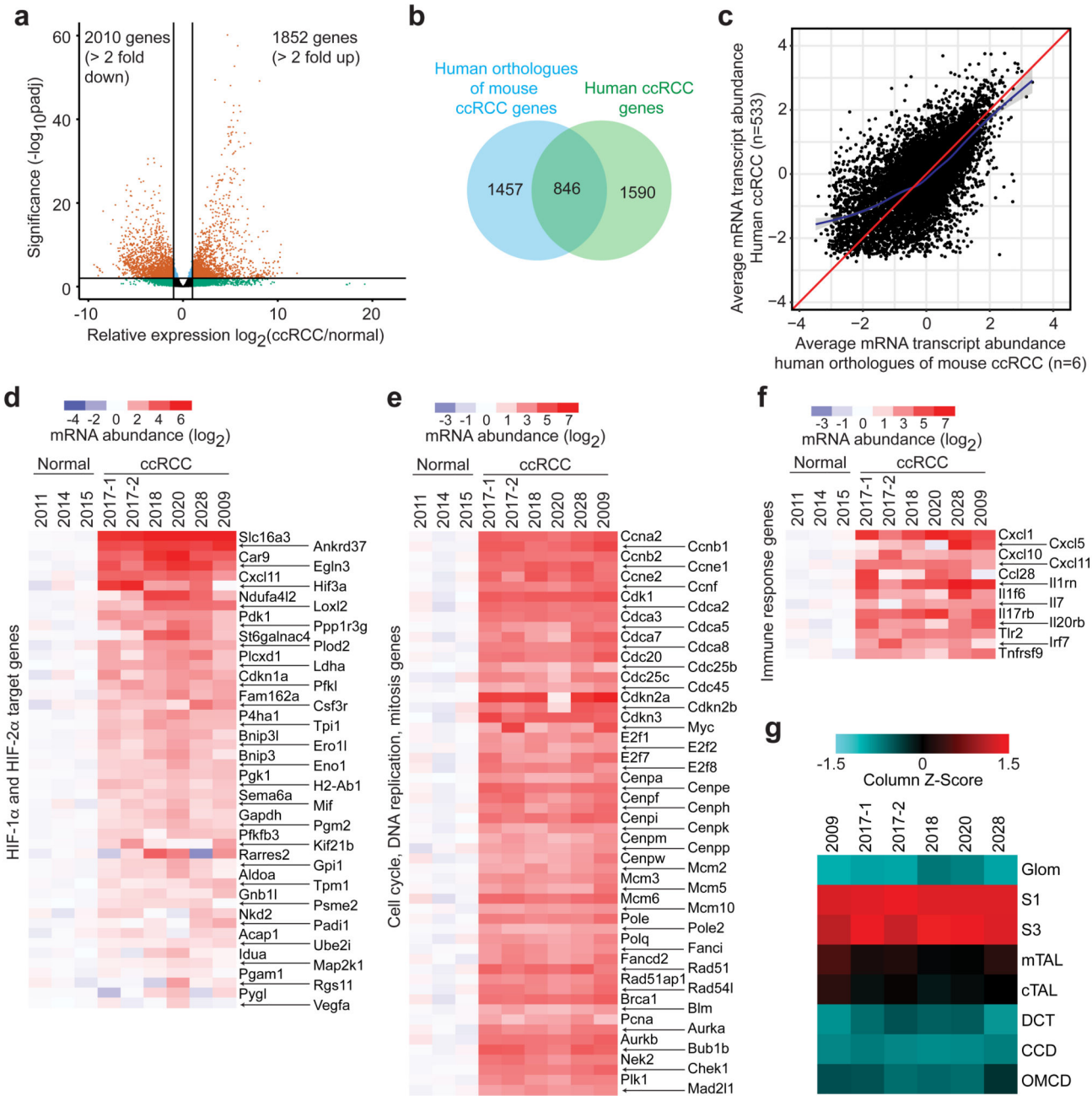

Figure 3. ccRCCs in $Vhl^{\Delta/\Delta}Trp53^{\Delta/\Delta}Rb1^{\Delta/\Delta}$ mice exhibit global transcriptional similarities to human ccRCCs

(**a**) Volcano plot showing statistically significantly (false discovery rate < 0.01, horizontal line) and differentially regulated genes (> 2-fold up- or down-regulated, vertical lines) between 6 mouse ccRCCs and 3 normal kidney cortex samples. (**b**) Venn diagram showing overlap of the human orthologues of the set of mouse differentially expressed genes with the set of differentially expressed genes derived from analysis of human normal kidney (n=72) and ccRCC (n=533) samples using the same criteria as for the analyses in **a**. (**c**) Sample-

averaged, normalised and log-transformed gene expression values for all unique orthologous gene pairs in human and mouse ccRCC (black dots). The red line represents a perfect correlation and the blue line results from a smooth parametric regression with confidence band in grey. Pearson coefficient [0.65;0.67] ($P < 1 \times 10^{-16}$), 95% confidence interval. (**d-f**) Mouse ccRCCs show upregulation of mRNA expression of (**d**) HIF-1α and HIF-2α target genes, (**e**) genes that regulate cell cycle progression, DNA replication and mitosis and (**f**) genes involved in immune responses. (**g**) Normalised Pearson correlation scores depicting global mRNA expression similarities between mouse ccRCCs and normal nephron segments; Glom = glomeruli, S1/S3 = proximal tubule S1 and S3 segments, mTAL/cTAL = medullary and cortical thick ascending limbs of Henle's loop, DCT = distal convoluted tubules, CCD/OMCD = cortical and outer medullary collecting ducts.

Europe PMC Funders Author Manuscripts

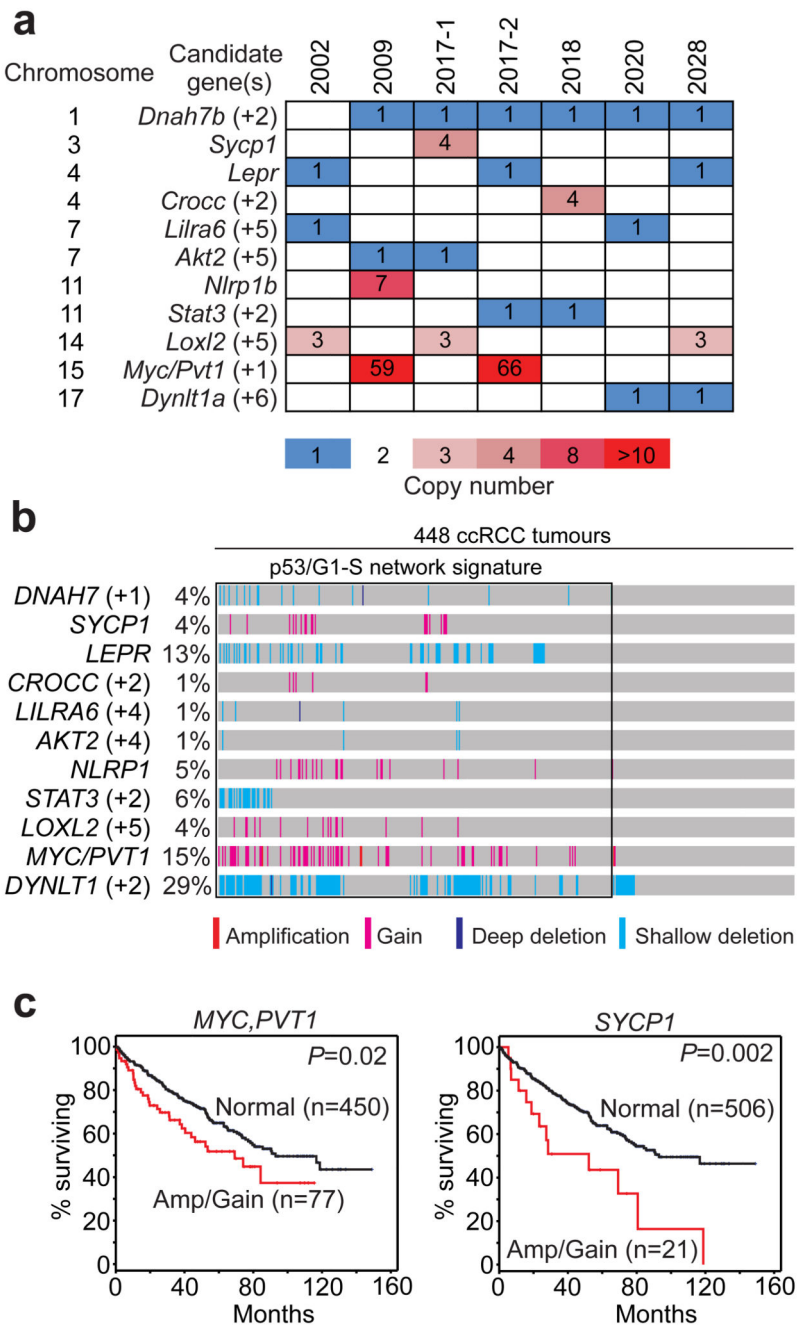

Figure 4. Copy number variations in mouse ccRCCs are also present in the p53/G1-S ccRCC subset of human ccRCCs

(**a**) Focal copy number alterations of the indicated genes/chromosomal regions in mouse ccRCCs. Numbers in parentheses represent the number of other named candidate genes in each region – see Supplementary Table 2 for the full gene lists (**b**) Distribution of copy number gains/amplifications of the human orthologues/syntenic chromosomal regions of mouse ccRCC gained genes and copy number losses of mouse ccRCC lost genes in 448 human ccRCC tumours. Numbers in parentheses represent the number of human orthologues of the mouse genes that are found in each chromosomal region. The sub-set of

the p53/G1-S network tumours is indicated by a box. (**c**) Survival curves of human ccRCCs harbouring copy number gains of the indicated genes. *P* values are from the Log-rank Mantel-Cox test.

Europe PMC Funders Author Manuscripts

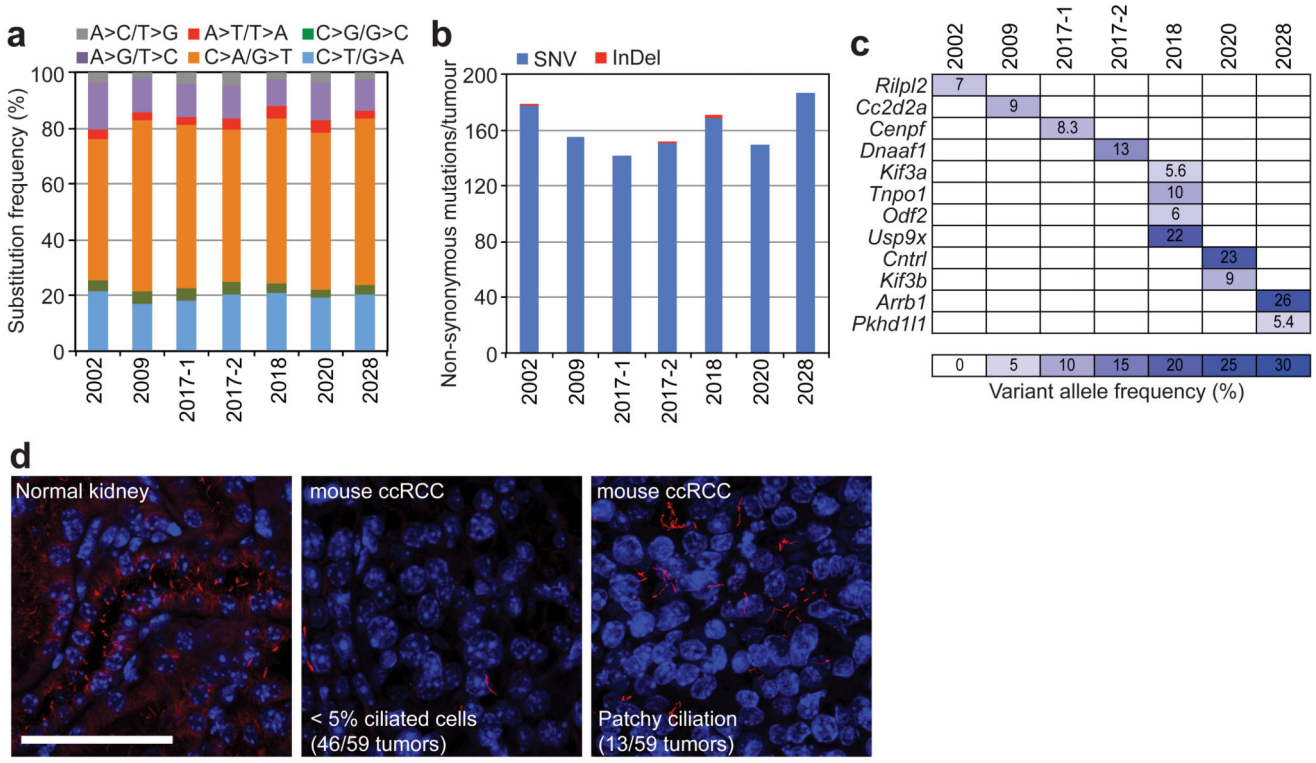

Figure 5. Exome sequencing reveals that mouse and human ccRCCs exhibit recurrent mutations of primary cilia-associated genes

(**a**) Distributions of nucleotide transitions and transversions in mouse ccRCCs. (**b**) Numbers of non-synonymous mutations caused by single nucleotide variations (SNVs) or insertions and deletions (InDels) in mouse ccRCCs. (**c**) Recurrent alterations in primary cilium-associated genes in mouse ccRCCs. Variant allele frequencies of each mutation are shown. (**d**) Examples of anti-acetylated tubulin staining to label primary cilia in normal kidney tissue and mouse ccRCCs. The frequency of tumours (n=59) showing these observed patterns is indicated. All panels are the same magnification, scale bar = 50 μm.

Europe PMC Funders Author Manuscripts

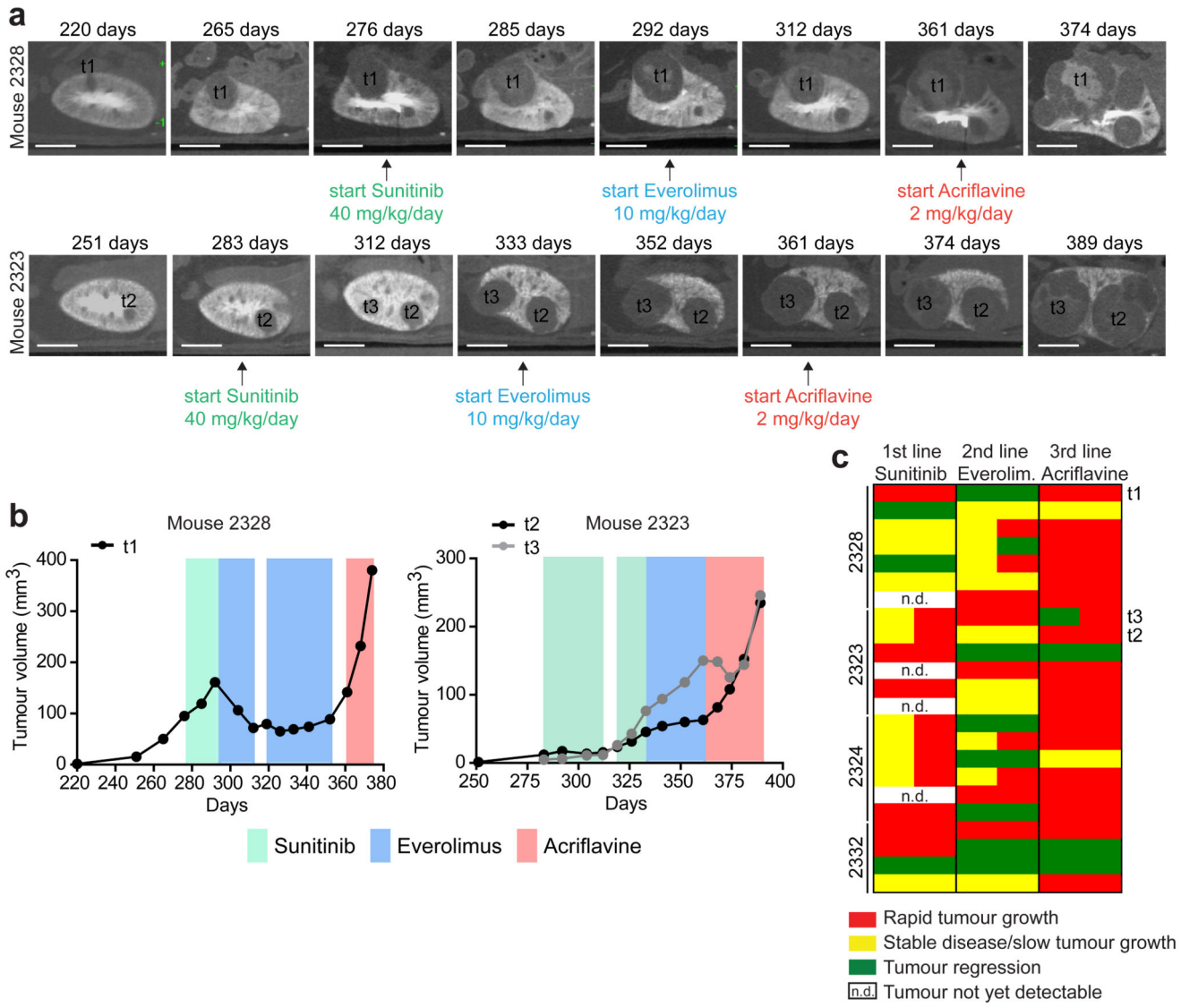

Figure 6. ccRCCs in $Vhl^{\Delta/\Delta}Trp53^{\Delta/\Delta}Rb1^{\Delta/\Delta}$ mice exhibit varying patterns of therapeutic sensitivity and resistance

(**a**) Examples of development of three tumours (t1, t2, t3) in two different mice before and during therapy, visualised with contrast assisted μCT imaging. Scale bars = 5 mm. (**b**) Quantification of volumes of t1, t2 and t3 from **a**. (**c**) Summary of therapeutic effects of Sunitinib, Everolimus and Acriflavine (each row represents an independent tumour) in four mice.